

Tropical Pacific internal atmospheric dynamics and resolution in a coupled GCM

Hosmay Lopez · Ben P. Kirtman

Received: 29 July 2013 / Accepted: 17 June 2014 / Published online: 26 June 2014
© Springer-Verlag Berlin Heidelberg 2014

Abstract A noise reduction technique, namely the interactive ensemble (IE) approach is adopted to reduce noise at the air–sea interface due to internal atmospheric dynamics in a state-of-the-art coupled general circulation model (CGCM). The IE technique uses multiple realization of atmospheric general circulation models coupled to a single ocean general circulation model. The ensembles mean fluxes from the atmospheric simulations are communicated to the ocean component. Each atmospheric simulation receives the same SST coming from the ocean component. The only difference among the atmospheric simulations comes from perturbed initial conditions, thus the atmospheric states are, in principle synoptically independent. The IE technique can be used to better understand the importance of weather noise forcing of natural variability such as El Niño Southern Oscillation (ENSO). To study the impact of weather noise and resolution in the context of a CGCM, two IE experiments are performed at different resolutions. Atmospheric resolution is an important issue since the noise statistics will depend on the spatial scales resolved. A simple formulation to extract atmospheric internal variability is presented. The results are compared to their respective control cases where internal atmospheric variability is left unchanged. The noise reduction has a major impact on the coupled simulation and the magnitude of this effect strongly depends on the horizontal resolution of the atmospheric component model. Specifically, applying the noise reduction technique reduces the overall climate variability more

effectively at higher resolution. This suggests that “weather noise” is more important in sustaining climate variability as resolution increases. ENSO statistics, dynamics, and phase asymmetry are all modified by the noise reduction, in particular ENSO becomes more regular with less phase asymmetry when noise is reduced. All these effects are more marked for the higher resolution case. In contrast, ENSO frequency is unchanged by the reduction in the weather noise, but its phase-locking to the annual cycle is strongly dependent on noise and resolution. At low resolution the noise structure is similar to the signal, whereas the spatial structure of the noise deviates from the spatial structure of the signal as resolution increases. It is also suggested that event-to-event differences are largely driven by atmospheric noise as opposed to chaotic dynamics within the context of the large-scale coupled system, suggesting that there is a well-defined “canonical” event.

Keywords ENSO · Couple models · Climate simulations · Atmospheric noise

1 Introduction

There are theories that argue that the irregularity of ENSO and ultimately the loss of predictability are largely driven by stochastic (internal atmospheric) noise forcing (e.g., Kirtman and Schopf 1998; Eckert and Latif 1997; Blanke et al. 1997; Penland and Matrosova 1994; Penland and Sardeshmukh 1995; Flügel and Chang 1996; Moore and Kleeman 1996; Kleeman and Moore 1997; Xue et al. 1997; Chen et al. 1997; Moore and Kleeman 1999a, b; Thompson and Battisti 2001; Kleeman et al. 2003; Flügel et al. 2004; Zavala-Garay et al. 2003a, b, 2004, 2005, 2008). If the stochastic forcing is of primary importance then it is

H. Lopez (✉) · B. P. Kirtman
Department of Meteorology and Physical Oceanography,
Rosenstiel School of Marine and Atmospheric Science,
University of Miami, 4600 Rickenbacker Causeway,
Miami, FL 33149, USA
e-mail: hlopez@rsmas.miami.edu

possible that the details (e.g., space–time structure and state dependence) of the noise are also important.

For example, Moore and Kleeman (1999a, b) calculated the stochastic optimal of an intermediate coupled model and argued that their spatial structure is consistent with the spatial structure associated with observed Westerly Wind Bursts (WWBs). That is, the space–time statistics of the stochastic forcing may be important in producing optimal growth (i.e., produce larger response in the coupled system). Kirtman and Shukla (2000) argued that wind stress noise associated with the Indian summer monsoon has a specific structure in the tropical Pacific that can trigger ENSO. Zavala-Garay et al. (2003a) found that perturbation growth due to stochastic forcing is more favorable over the western/central Pacific where SST is moderately warm and more sensitive to noise forcing. There are many studies pointing at the importance of noise in triggering ENSO events. Larson and Kirtman (2013) argued that the low-frequency component of the noise is more important and serve as trigger to ENSO as oppose to high frequency noise. Other example of ENSO trigger includes the Pacific Meridional Model (Chang et al. 2007a, b; Zhang et al. 2009a, b). This mode of variability is associated with westerly wind anomalies over the central Pacific subtropics along with peak SSTA during boreal spring (Chiang and Vimont 2004).

The understanding of the importance of stochastic forcing is complicated by the possibility that it may be state dependent. A case in point is the results of Kirtman et al. (2005) who found that the spatial structure of the dominant wind stress noise was remarkably similar to the spatial structure of the coupled signal and that the noise was state dependent. Jin et al. (2007) formulated a simple coupled model to examine how state independent noise versus state dependent noise affected ENSO variability. In that study, they found that unlike for state-independent noise, when the noise is state-dependent, it alters the ensemble mean evolution of ENSO, and also amplifies the ensemble spread during ensemble forecast. In a modeling study, Lopez et al. (2013) found that state-independent noise (i.e., noise with stationary space–time statistics) has little effect in modulating ENSO and tropical Pacific variability. In contrast, they found significant impact on ENSO when the noise is state-dependent.

Examples (non-exhaustive) of state independent and dependent noise are as follows:

1. The Madden-Julian oscillation (MJO; Chen et al. 1996): Zhang and Gottschalck (2002) indicated a tendency for larger SST anomalies of ENSO warm events in the eastern Pacific, to be preceded by stronger oceanic Kelvin wave anomalies induced by the MJO in the western Pacific.
2. Cold surges from mid-latitude over the western Pacific (Love 1985; Chu 1988; Kiladis 1994): Yu and Rienecker (1998) indicated in their case study of the 1997–1998 El Niño that Westerly Wind Bursts (WWBs) were associated with cyclones induced by a northerly surge. Yu et al. (2003) showed that changes in northerly surge pathways, influenced by ENSO phases, were related to WWBs occurrences through cyclone formations over the western Pacific. WWBs can result from tropical cyclones (Keen 1982; Yu and Rienecker 1998).
3. WWBs associated with twin cyclones over the western Pacific, accelerated the development of the 1986–1987 El-Niño event (Nitta and Motoki 1987; Nitta 1989). Murakami and Sumathipala (1989) emphasized that collective occurrences of WWBs lasting 7–20 days over the western Pacific were related to ENSO.
4. Larson and Kirtman (2013) found that the Pacific Meridional Mode (PMM) appears to be an effective trigger of ENSO events when the western-to-central Pacific is preconditioned (i.e., anomalously high sea surface heights or heat content).
5. Other sources of stochastic noise forcing are: Indian summer monsoons (Kirtman and Shukla 2000) and midlatitude atmospheric variability (Vimont et al. 2003a, b).

Throughout this paper we will refer to variability due to atmospheric internal dynamics as noise. The goal of this study is to understand how internal atmospheric dynamics affects the coupled climate system at different resolutions. This is an interesting question, given that the ocean response may depend on the space–time structure of the noise forcing, and as noted above, the statistics of the noise is likely to be dependent on atmospheric model resolution. In order to tackle this question we will make use of the Interactive Ensemble (IE) coupling strategy proposed by Kirtman and Shukla (2002) and applied to CCSM3 (Kirtman 2009; Kirtman et al. 2011), so that any signal dependence in the noise statistics is retained. The IE technique was specifically developed with the purpose of studying the relative importance of stochastic (weather noise) forcing and deterministic coupling in generating climate variability in CGCMs. This noise reduction technique is different from the a posteriori ensemble averaging of multiple coupled model realizations in that the ensemble averaging is done to the atmospheric fluxes as the CGCM evolves, therefore it is viewed as fully interactive. Using the IE technique Kirtman and Shukla (2002) suggested that noise reduction only slightly decreased the amplitude of ENSO in the COLA anomaly coupled model (Kirtman et al. 2002), shortened its periodicity, and increased its regularity. In a separated IE study, Yeh and Kirtman

(2004a, b) diagnosed SST variability in the North Pacific and argued that the local effect of noise forcing dominated the variability and blurred the tropical-midlatitude SST teleconnections. That is, the teleconnection is still present, but the amplitude of the local noise is much larger. Wu and Kirtman (2004a, b) made use of the IE technique to isolate the importance of coupled air-sea feedbacks over warm tropical oceans for monsoon-global ocean teleconnections.

In the context of this paper, we refer to noise as the stochastic component of atmospheric fluxes at the air-sea interface. Whereas in most of the previous work, stochastic forcing was externally prescribed and derived as some approximation to weather noise statistics that is state independent. The difference here is that weather noise is internally produced by the atmospheric model and is state dependent. The goals/purposes of this paper are to:

1. Understand how ENSO is affected by internal atmospheric dynamics and how atmospheric model resolution might influence these interactions;
2. Diagnose the role of atmospheric noise in the diversity of ENSO, including event-to-event and phase (warm-to-cold) asymmetry;
3. Examine the role the signal plays (if any) in modifying noise amplitude and spatial structure at different resolution.

The first point is a general issue that will be discussed throughout this study. The second point is mainly aiming at the importance of noise forcing in sustaining/modifying/diversifying what is often called “signal”. The third point is attempting at understanding the role of the signal modulating the noise, namely signal dependent noise.

The rest of this paper is organized as follows: Sect. 2 describes observational estimates and the coupled model used for this study. The interactive ensemble technique is briefly discussed in Sect. 3. Section 4 discusses the effect of noise reduction on the mean state. Section 5 highlights the effect of noise reduction in tropical Pacific variability, including the effect of noise on ENSO statistics, dynamics, and phase asymmetry with and without noise reduction. An analysis of the structure of noise is also presented in this section. A summary and discussion section is also included as Sect. 6.

2 Observation datasets and the coupled model

The SST is taken from the reconstructed Reynolds and Smith (1994), with a horizontal resolution of 2° (~ 220 km) and period from January 1950 to December 2001. The CGCM used in this work is the Community Climate System Model version 3 (CCSM3) from the National Center for Atmosphere Research (NCAR). This

model is an earth system model comprised of four geophysical components consisting of atmosphere, land, ocean, and sea ice components all linked by a flux coupler. The coupler exchanges information among the components interactively while the model is running. The atmosphere is modeled by the Community Atmosphere Model version 3 (CAM3). The land surface is modeled by the Community Land Surface Model version 3.0 (CLM3). The oceans are represented using the Parallel Ocean Program version 1.4.3 (POP) and the sea ice is modeled by the Community Sea Ice version 5 (CSIM5).

In this work, CAM3 and CLM3 have horizontal resolution of T42 (128 longitude and 64 latitude points, or ~ 280 km) for the low-resolution case and T85 (256 longitude and 128 latitude points, or ~ 140 km) for the medium resolution case. There are 26 atmospheric vertical levels for all experiments. For the POP and CSIM5, the horizontal resolution is approximately 1° in the longitude and variable in the latitude direction with finer resolution, about $1^\circ/3^\circ$, near the equator. The POP has 40 vertical levels with level thickness monotonically increasing from approximately 10–250 m with depth. For each model run presented here, the initial conditions are taken from previous model run after spinup. The model is further integrated for hundreds of years with only the last 200 years employed for the analysis.

CCSM3 uses a daily coupling interval for the ocean component and an hourly coupling frequency for the other components of the climate system. Air-sea coupling is conservatively and communicating momentum, heat, fresh water, sensible, latent, and radiative heat fluxes between the ocean and atmosphere. At every hour, the atmosphere component communicates to the coupler average wind speed, humidity, potential temperature, precipitation, air density, geopotential height of the lowest grid level, fluxes of net surface solar and long-wave radiation. The ocean component sends the coupler the upper-level time-averaged temperature and velocity at the end of the coupling period. With these inputs from the ocean and atmosphere, the coupler calculates momentum, heat, and fresh water fluxes hourly, and then passes them to the ocean model as daily means.

A detailed description of CCSM3 simulation of ENSO is found in Collins et al. (2006) and for ENSO prediction in Kirtman and Min (2009). Here, some of the most relevant issues with this model are highlighted. Interannual SSTA associated with ENSO extend too far to the west in CCSM3 as compared to observations. This is consistent with the well-documented westward displacement of the mean eastern Pacific cold tongue position. The SSTA also show a strong meridional confinement about the equator as compared to observations. This confinement can be the result of significantly narrow zonal wind stress forcing in CCSM3.

Deser et al. (2006) found that the meridional confinement of zonal wind stress is related to the high frequency of interannual variability in CCSM3, and the mechanism for this is described in Kirtman (1997). Despite the well-known errors in ENSO statistics, CCSM3 has also been shown to have reasonable ENSO prediction skill. For instance, Kirtman and Min (2009) compared CCSM3 ENSO predictions to the operational NOAA Climate Forecasting System (CFS), and found that the both the deterministic and probabilistic forecast quality in the Nino3.4 region was comparable.

3 The Interactive Ensemble technique

The IE strategy has been used to diagnose the ENSO-Monsoon relationship (Wu and Kirtman 2003) and mechanisms for low-frequency SST variability (Yeh and Kirtman 2004a, b; Wu et al. 2004; Schneider and Fan 2007) among others. It uses multiple realizations of the atmospheric model (CAM) coupled to a single realization of the ocean model (POP), a single realization of the sea-ice model and a single realization of the land-surface model. The coupling of the multiple realizations of CAM to the single realizations of the other component models is accomplished through the CCSM coupler. The purpose of this coupling strategy is to significantly reduce the stochastic forcing of the ocean due to internal atmospheric dynamics. Ensemble averaging of fluxes of heat, momentum and fresh water produced by the individual CAM ensemble members before they are passed to POP effectively filters the noise in the fluxes due to internal atmospheric dynamics. The sea-ice and land surface models are also coupled to the ensemble mean fluxes. Additional details can be found in Kirtman (2009).

The interactive ensemble strategy works as follows (Fig. 1 of Kirtman et al. 2005). Each realization of CAM is statistically identical; the only difference among the CAM ensemble members is the initial condition. Because the atmosphere is sensitively dependent on initial conditions, the CAM realizations evolve differently. As the interactive ensemble evolves, each CAM realization experiences the same SST predicted by the ocean component. POP, on the other hand, experiences surface fluxes of heat, momentum and freshwater that are the ensemble average of the CAM realizations. The CAM realizations are noise independent (i.e., the noise among the ensemble members is uncorrelated), but since they are all coupled to the same SST, they have the same SST forced signal. The interactive ensemble coupling does not modify the internal dynamics of the individual CAM realizations, up to any changes in the mean state and the character of the SST variability. This is because the ensemble averaging is only applied to the

fluxes of heat, momentum and freshwater as they are passed to the ocean component. In our experiments, both low and medium-resolution IE are implemented using six atmospheric GCMs realizations.

4 Impact of IE on the mean state

Here, we discuss the impact of applying the IE to the low and medium resolution atmospheric component models, with the ocean having the same 1° resolution (see Sect. 2). We compare 200-year simulations of the control and its respective IE (see Table 1 for experiment description). We remind the reader that any differences between control and the IE experiment in CCSM3 is assumed to be caused by internal atmospheric dynamics—we cannot completely eliminate the possibility of non-linearity in, for example, the signal or the mean state.

Here we primarily focus on climate variability, but as noted above it is also possible that the mean climate could be affected, and could contribute to the differences in the simulations. This is because the coupled model is “tuned” using only one atmospheric GCM, and reducing noise can have a rectified effect on the mean (see also Kirtman 2009; Kirtman et al. 2011). Figure 1, for example, shows the mean SST along the equatorial Pacific, for both low and medium-resolution control and IE simulations along with observational estimates. The general SST gradient is captured in all simulations, and is fairly consistent among the simulations. Notable differences are in the far western Pacific and far eastern Pacific. For example, the warm pool bias appears (or more precisely the warm SST plateau in the west Pacific) to be reduced in both simulations with IE. Note that the medium-resolution (T85-control) experiment does the worst job in depicting the SST plateau west of 160E. The T42-control simulation has a large warm bias in the far west of the basin, but there is some hint of an SST plateau around 140E. It should be noted we are not arguing that the IE is the way to improve the simulation in the west Pacific, but rather it provides a potential mechanistic understanding of the source of the warm pool bias.

Table 1 Experiments description

Experiment	Description	Atmosphere resolution
T42-CTL	Low resolution control	T42 (~ 2.8°)
T42-IE	Low resolution interactive ensemble	T42 (~ 2.8°)
T85-CTL	Mid resolution control	T85 (~ 1.4°)
T85-IE	Mid resolution interactive ensemble	T85 (~ 1.4°)

The ocean resolution is the same for all experiments

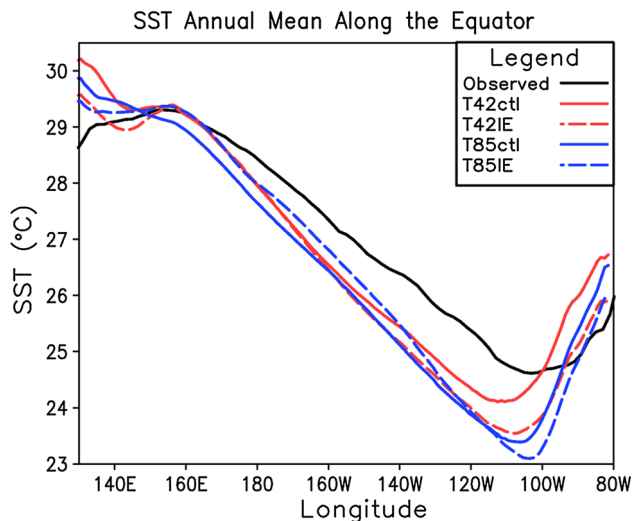


Fig. 1 Equatorial mean seas surface temperature (SST, °C) from observed estimates and the four CCSM3 experiments. The *horizontal axis* corresponds to longitude across the Pacific Ocean

The application of IE also slightly reduces the SST bias just off the coast of South America. This is also true irrespective of the resolutions examined here. A region where IE degrades the mean climate is in the cold tongue, especially between 120 W and 90 W. Note that T85 IE is arguably the worst simulation in this region with cold bias of about 2 °C. It appears that the IE tends to improve the simulation in regions where the atmosphere strongly forces the ocean (e.g. warm pool region), whereas it degrades simulation in other regions (e.g. cold tongue). This degradation or improvement may be model dependent, but is not resolution dependent in this model.

There are a few physical mechanisms by which atmospheric noise affects SST. Over the equatorial western Pacific, the mean thermocline is considerably deep; therefore thermocline dynamics has little effect on the surface temperature. Changes in SST over this region are more related to mixed-layer processes. SST changes in this region can be influenced by air-sea heat fluxes, temperature advection by currents (both geostrophic and Ekman components), radiative fluxes at the bottom of the mixed layer to the ocean interior, entrainment, and diffusion. All of these can be influenced by atmospheric noise. For example, stirring by surface winds can enhance latent and sensible heat fluxes, reducing buoyancy and SST. Entrainment of water from below the mixed layer is influenced by turbulent kinetic energy balance, which is related to wind stirring and surface heating. The impact of atmospheric noise on SST over the eastern Pacific is more related to thermocline dynamics. The thermocline there is very shallow therefore downwelling/upwelling Kelvin waves have significant effects on the surface response. These waves can be generated by atmospheric noise in the wind stress (e.g., WWBs).

5 Tropical Pacific variability and IE

Before looking at how ENSO is modified by IE, we analyze in general, variability in the tropical Pacific. An analysis of variance is performed for SSTA, zonal wind stress (τ_x), and precipitation. Variance is calculated using anomalies obtained by removing the climatological annual cycle from each field. The variances for precipitation and τ_x are calculated from the ensemble mean of those fields, which is used to force the ocean component. Figure 2 shows the standard deviation for SST, zonal wind stress and precipitation for the control models at different resolution. SST variability is slightly larger at T42ctl and extends further westward compared to T85ctl. This was also noted in Deser et al. (2006). The zonal wind stress variability is similar in both models and is dominated by extratropical variance. The precipitation pattern has a sideways “v” structure with maximum variability over the warm pool and away from the equator.

Figure 3 shows the standard deviation ratio (i.e., σ_{IE}/σ_{CTL}) for IE divided by control for both T42 and T85 simulations. Shaded contours indicate 99 % statistical significant based on F-test with smaller values indicating regions of large variance reduction—the results are statistically significant almost everywhere. Overall, the SST standard deviation ratio (IE/control) ranges from 0.5 at T85 and to about 0.65 for T42 in the equatorial Pacific. This ratio is a useful diagnostic for quantifying the coupled feedback strength. That is, Kirtman et al. (2005) demonstrated that when the standard deviation ratio is greater than 1.0, unstable coupled feedback and non-linear dynamics are likely important in forcing SST variability. When the ratio falls between 0.4 and 1.0, unstable coupled feedbacks, non-linearity, or ocean dynamics may play a significant role. When this ratio is less than 0.4, SST variability is mostly due to atmospheric noise forcing alone. This critical standard deviation ratio of 0.4 (i.e., 1/6 variance ratio) is based on six atmospheric ensemble members. Non-linearity and coupled feedbacks are likely to be important in determining the dynamical regime of CCSM3 as described in Kirtman (2009).

The differences in variance reduction between the medium (0.5) and low (0.65) resolution simulations are also statistical significant at 99 % confidence level based on an *F* test. This, along with Fig. 3 suggests that the variability in the T85 control case is more noise dependent than the T42 control, i.e., the variance reduction at T85 is larger than T42. Most of the reduction in variance occurs away from the equator for both resolutions. This is generally seen by considerable lower standard deviation ratios away from the equator.

In the deep tropical Pacific at T42, the spatial structure of the standard deviation ratio (σ_{IE}/σ_{CTL}) for SSTA and

Fig. 2 Standard deviation of SST ($^{\circ}\text{C}$), zonal wind stress (10^{-1} N m^{-2}), and precipitation (mm) for control models at different resolution. Standard deviation is calculated from interannual anomaly defined by removing model climatology

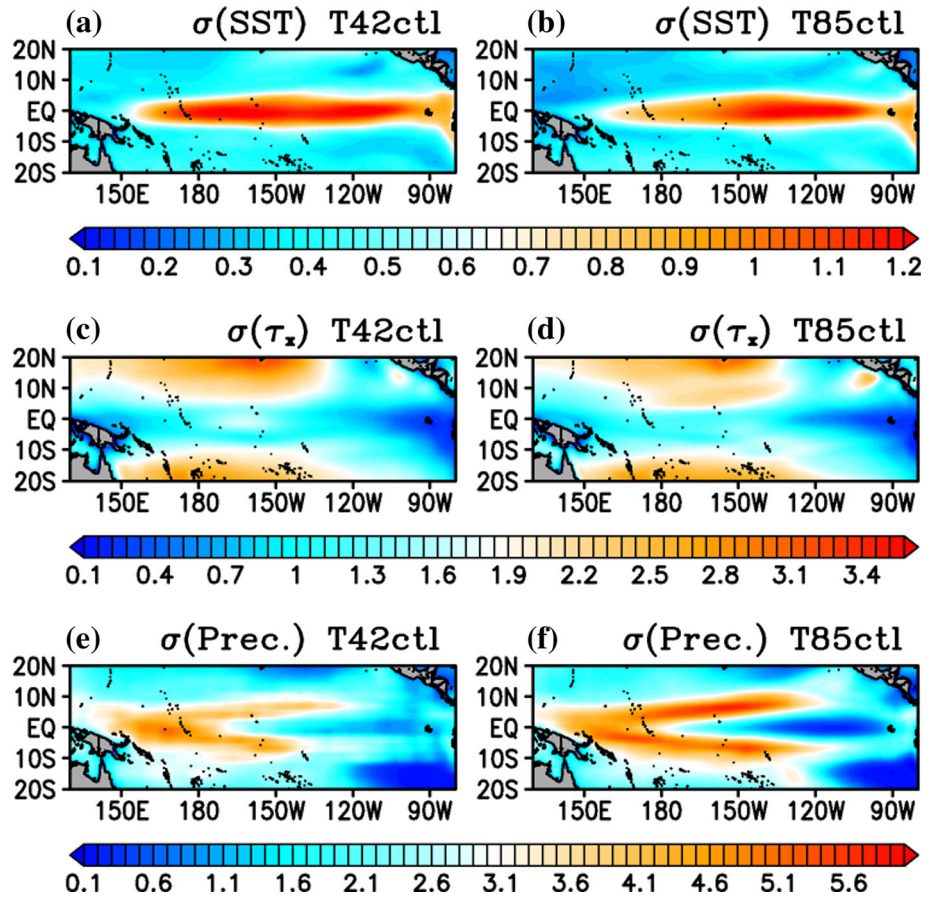
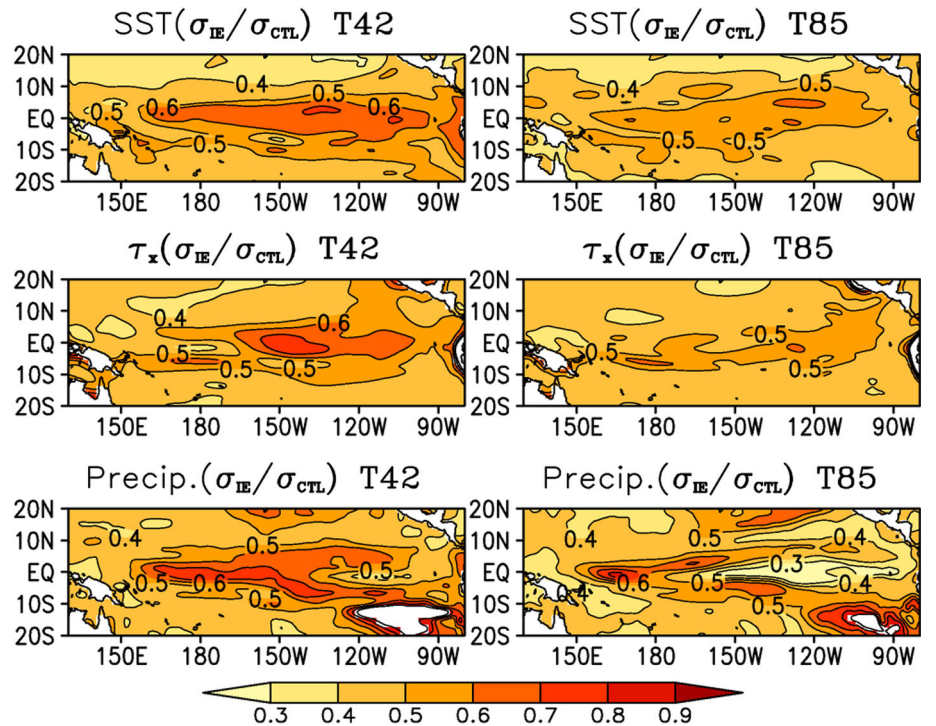


Fig. 3 SST (top), zonal wind stress (middle), and precipitation (bottom) standard deviation ratio along the tropical Pacific sector. The ratio is defined as IE divided by the control experiment for T42 (left) and T85 (right) resolution cases. Shaded contours indicate 99 % statistical significance using an *F* test



zonal wind stress resembles the spatial structure of the control standard deviation (i.e., Fig. 2). This is in contrast to T85 where the variance reduction has a distinctly different spatial structure than the control standard deviation. The T42 results presented here are consistent with the Kirtman et al. (2005) results for the COLA T42 model in that the dominant noise patterns largely projected on the “signal” patterns. As resolution increases the dominant noise structures start to deviate from the signal patterns significantly. This will be discussed in more detail later in the paper.

Similar to the SST, the variance reduction for the wind stress and precipitation is more marked for T85 case (i.e., lower values of variance fraction). Most of the region shows values <0.5 for wind stress. The precipitation structure is more complicated, it has values close to 1 over the southeast tropical Pacific “ocean desert” region for both resolutions. This is mostly due to very small precipitation variances in both simulations. An interesting pattern emerges at T85 with ratios <0.3 over the cold tongue. This is a region of very cold SST bias (Fig. 1) for T85 IE case, which may be playing a role in suppressing noise-induced variability or in reducing the noise.

5.1 ENSO characteristics: variance

In this Section we diagnose how the IE implementation affects ENSO at different resolutions. Table 2 provides a quantitative comparison of Niño3.4 SSTA by showing the second, third, and four statistical moments with their respective confidence interval at a 99 and 95 % level. The observed standard deviation is $0.83\text{ }^{\circ}\text{C}$. The two control experiments suggest higher than observed variability of ENSO, with the medium resolution being closer to observed (e.g., $\sigma_{T42CTL} = 0.91\text{ }^{\circ}\text{C}$ and $\sigma_{T85CTL} = 0.88\text{ }^{\circ}\text{C}$); this is consistent with Deser et al. (2006). Implementing the IE noise reduction technique consistently reduces ENSO variability (e.g., $\sigma_{T42IE} = 0.58\text{ }^{\circ}\text{C}$ and $\sigma_{T85IE} = 0.51\text{ }^{\circ}\text{C}$), and this is consistent with Figs. 2 and 3 discussed above. The differences in standard deviation discussed before are statistically significant at 99 % confidence level for all cases. The higher resolution case is the most affected by IE. The

positive skewness of the observed ENSO is described by the third moment. Note that the low-resolution control is negatively skewed (significant to a 99 % level). A near-zero skewness is obtained by the noise reduction at T42. Differences in the third moment for the T85 cases are also statistically significant. Comparison for the fourth moment for all cases is not obvious due to a lack of statistical significance. Irrespective of resolution, internal atmospheric dynamics is a key component in determining the overall shape of the PDF. The dominant periodicity, as detected from the Niño3.4 power spectra (not shown), is not modified by the interactive ensemble coupling.

Figure 4 shows the variance by calendar month associated with Niño3.4 SST anomaly. The solid-black line depicts observed estimates, whereas the various simulations are noted in the legend. All the experiments agree, in a general sense, there is a reduction in variance during the boreal spring, and the two IE experiments show an overall reduction in variance compared to the control that is consistent with Fig. 3. Atmospheric resolution affects the seasonal variations in variance. This is particular pronounced during late boreal spring and boreal summer where the two control variances are relatively similar, but the T85 IE variance is considerably smaller than the T42 IE variance. Most of the enhanced reduction of variance associated with T85 IE seen in Fig. 3 appears to be associated with this limited period of the annual cycle. This is a season often characterized by low signal-to-noise ratio; this may suggest that SST variability during this period is mostly noise induced. We will also come back to this issue later in the paper.

5.2 ENSO composite evolution

Here we explore the effects of atmospheric noise in terms of the evolution of composite of warm and cold events. The composite analysis is based on the warm and cold events that have a December–January–February (DJF) Niño3.4 SSTA greater than one standard deviation. Based on this threshold and that we have about 200 years of monthly data from all cases, the composite includes more than 40 events both warm and cold from each experiments.

Table 2 Second, third, and four statistical moments associated with Niño3.4 SSTA described by the probability density function (PDF) on Fig. 12

	Observed	Experiment			
		T42ctl	T42 IE	T85ctl	T85 IE
StDev	$0.83 \pm 0.05(0.04)$	$0.91 \pm 0.03(0.02)$	$0.58 \pm 0.02(0.01)$	$0.88 \pm 0.03(0.02)$	$0.51 \pm 0.02(0.01)$
Skewness	$0.278 \pm 0.21(0.14)$	$-0.22 \pm 0.09(0.07)$	$-0.088 \pm 0.11(0.08)$	$0.097 \pm 0.098(0.07)$	$-0.117 \pm 0.11(0.08)$
Kurtosis	$0.055 \pm 0.34(0.24)$	$-0.296 \pm 0.17(0.12)$	$0.078 \pm 0.18(0.13)$	$-0.180 \pm .019(0.14)$	$0.0524 \pm 0.18(0.13)$

The statistical significant interval is also shown to a 99 % (95 %) confidence level

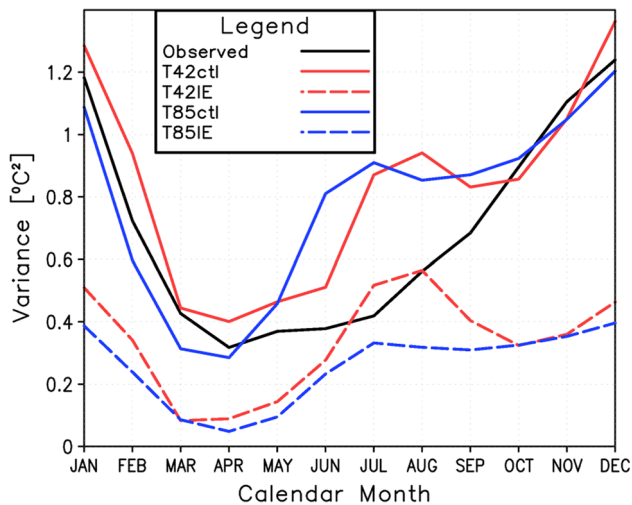


Fig. 4 Seasonality of SST anomaly variance over the Niño3.4 region for observed and model experiments. Anomaly is defined as the deviation from the seasonal mean

Figure 5 shows the lag/lead composite warm events for T42ctl (top-left), T42 IE (top-right), T85ctl (bottom-left), and T85 IE (bottom-right). The panels represent SSTA evolution from March of year 0 (leading to the extreme event) to May of year +1 (after the event). Notably the T42ctl simulation has stronger warm anomalies in the western Pacific that first appear in mid-summer and persist through the fall. In the T42ctl simulation, the warm SSTA begin to emerge by late May(0) and migrate westward until reaching a maximum extent in January(+1). The maximum T42ctl SSTA ($\sim 1.8^\circ\text{C}$) is located in the Niño3.4 region with a hint of eastward propagation. This maximum occurs during DJF and is also associated with significant activity in precipitation and zonal wind stress (not shown). Just like for the T42ctl case, Fig. 5 (bottom-left) shows the composite for T85ctl. The warm SSTA begin to emerge around April(0) which is about 2 months earlier than those at T42 resolution, then they propagate westward reaching maximum amplitude and western extent during boreal winter. Interesting, the El Niño amplitude is $\sim 0.2^\circ\text{C}$ warmer at T85 than at T42 case whereas for the cold (La Niña) cases (not shown) T42 has slightly larger amplitude. The results on ENSO phase asymmetry will also be discussed later.

The noise-reduced warm events composite are shown for T42 IE (Fig. 5 top-right) and T85 IE (Fig. 5 bottom-right). Applying the IE noise reduction technique at higher resolution (Fig. 5 bottom) leads to a significant reduction in amplitude, which is consistent with the standard deviation ratios shown in Fig. 2. In fact, as the variance analysis indicates, the reduced atmospheric noise at the air-sea interface has a greater effect on the composite at higher atmospheric model resolution. There are additional points to note in the bottom-right panel of Fig. 5. First, there is a

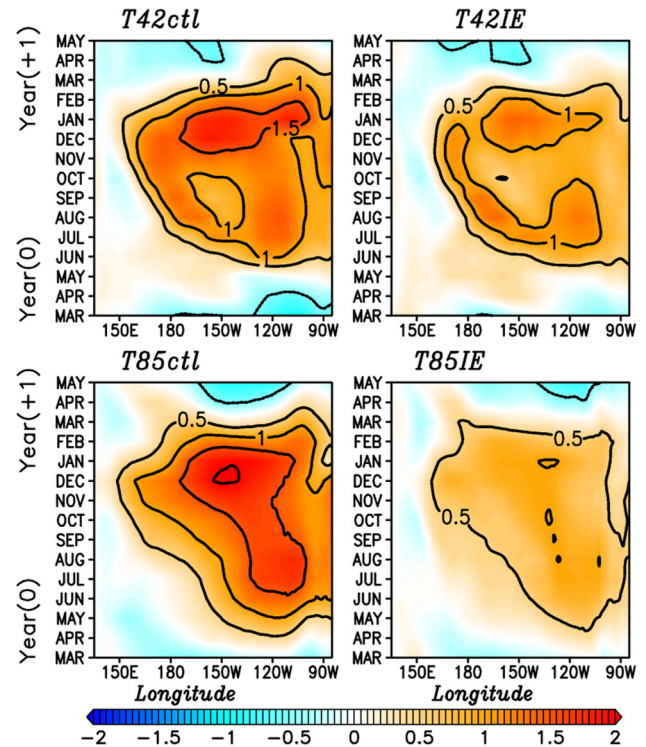


Fig. 5 Hovmöller diagram of composite analysis for warm (El Niño) events greater than one standard deviation. The horizontal axis corresponds to longitude across the equatorial Pacific Ocean. The vertical axis correspond to lead time in months, where year (0) is prior and year (1) is post the peak event. Composite based on Niño3.4 sea surface temperature anomaly (SSTA, $^\circ\text{C}$) centered on December–January–February

lack of a well-defined maximum in the composites, suggesting that the phase locking to the annual cycle is weakened in the T85 IE simulation. Second, as in T85ctl, SSTA first emerges during April (0), which is earlier than at T42. This suggests that any difference in when the initial SSTA emerges is independent of atmospheric internal variability and probably more related to other processes that are sensitive to atmospheric model resolution.

The robustness of the composite warm events is assessed in Fig. 6 (left column) and cold events (right column). The motivation is that we seek to document how much of the differences among events can be attributed to noise at the air-sea interface and how much is due fundamental non-linearity within the context of the coupled system. The spread among events in the above composite is also shown in Fig. 6 along with estimates of the deviations about the composite mean. The events represent the Niño3.4 SSTA evolution from early boreal spring to the following spring. Overall, there is considerable spread for warm events in T42ctl with only a few events peaking earlier or later than the ensemble mean peak in DJF. For T42 IE, there is a noted reduction in the spread as well as the amplitude of events. Also noted is the flattening of the ensemble mean

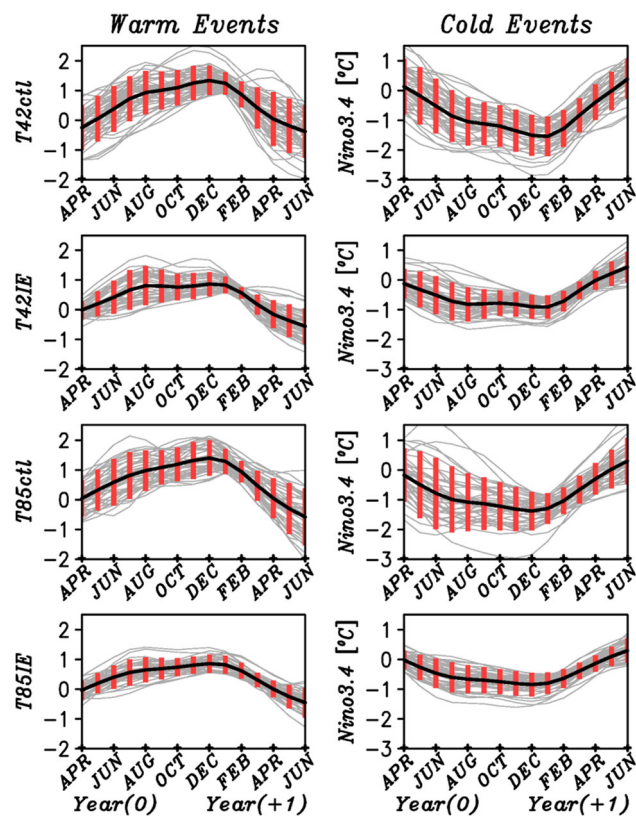


Fig. 6 Composite analysis of Niño3.4 SST anomaly evolution during warm (left-column) and cold (right-column) events. Composite is based on December–January–February Niño3.4 SST anomaly greater (less) than one standard deviation for warm (cold) events. The composite expands from boreal spring of the year (0) leading to the event to the following spring. Showing all individual events (grey-thin line), the ensemble mean of events (black-thick line), and the spread of events (red bars)

curved without a well define peak season. Most of the spread for T42ctl is observed from late boreal spring through fall leading to the DJF composite ENSO peak. This is in contrast with T42 IE where there is an indication of preferentially larger relative spread during boreal summer, which is associated with flattening of composite SSTA from August to the following January.

The T85ctl has similar features as those discussed for T42ctl. The spread for both control cases are of similar magnitude. For T85 IE, the ensemble mean of events are even flatter than those from T42 IE. Also, there is a more marked reduction in the spread; basically most warm events for this case evolve similarly without a well-defined peak. The overall impression from Fig. 6 is that noise at the air-sea interface has a larger role in the differences among warm events in the T85 model compared to the T42 model.

If atmospheric noise is state-dependent, then we might expect that the noise reduction associated with IE will be different for cold events. For this, we repeat the composite analysis but for La Niña cases (Fig. 6 right column).

Similar to the warm events, the T42ctl case shows significant spread among events compared to the T42 IE case. In contrast to warm events, the spread for T42ctl is consistently large throughout the evolution of the cold event. The T85ctl cold composite has the largest spread among the experiments and all warm and cold composites. For this case, there is significantly large spread early in the evolution of the event (e.g., May-to-July). Similar to the warm events, the ensemble mean of cold events evolution is flatter for the IE cases compared to the corresponding control. The T85 IE model produces the least spread with most cold events evolving similarly.

As previously mentioned, the noise reduction has a larger impact in the T85 model. In addition, it appears to have an asymmetric effect, with the La Niña phase being more affected than the El Niño phase. As further evidence of the asymmetric effect of the noise reduction we computed the change in spread for warm and cold events. For this, a mean spread value is found by averaging the spread for all months of the composite in Fig. 6 for each case and ENSO phase. For warm events, the spread of IE experiment is 46 % of the control experiment at T42 (i.e., ratio of IE/CTL). In contrast the change in spread is 40 % at T85. Similarly, the spread for cold events of T42 IE case is only 27 % of the control and T85 IE is 23 % of control.

5.3 ENSO phase asymmetry

Figures 1, 2, 3, 4, 5 and 6 have provided an overall picture how the IE coupling affects the variability in the tropical Pacific and the evolution of ENSO as a function of atmospheric model resolution. We also identified three issues that we require more in depth analysis, namely: (1) the structural similarities or differences between the signal and the noise (see Fig. 3 and associated discussion); (2) the sensitivity of the annual cycle of variance to IE coupling and resolution (see Fig. 4 particularly in late boreal spring and summer); and (3) the differences in the effects of the IE coupling on ENSO phase asymmetry. We address these issues in reverse order and begin this sub-section with a more in depth analysis of the phase asymmetry (i.e., issue 3; particularly Fig. 9). The annual cycle sensitivity is addressed in more detail in the discussion of Fig. 11 (i.e., issue 2) and spatial structure issues are diagnosed in the discussion of Fig. 14 at the end of the sub-section.

To study the impact of noise forcing and resolution on ENSO phase asymmetry, the composite analysis discussed above is used to examine the differences between warm and cold events. Warm and cold events greater than one standard deviation are averaged. Then, the symmetric (asymmetric) ENSO response is defined by subtracting (adding) the warm composite to the cold composite. Due to the opposite polarity of warm and cold phase, the

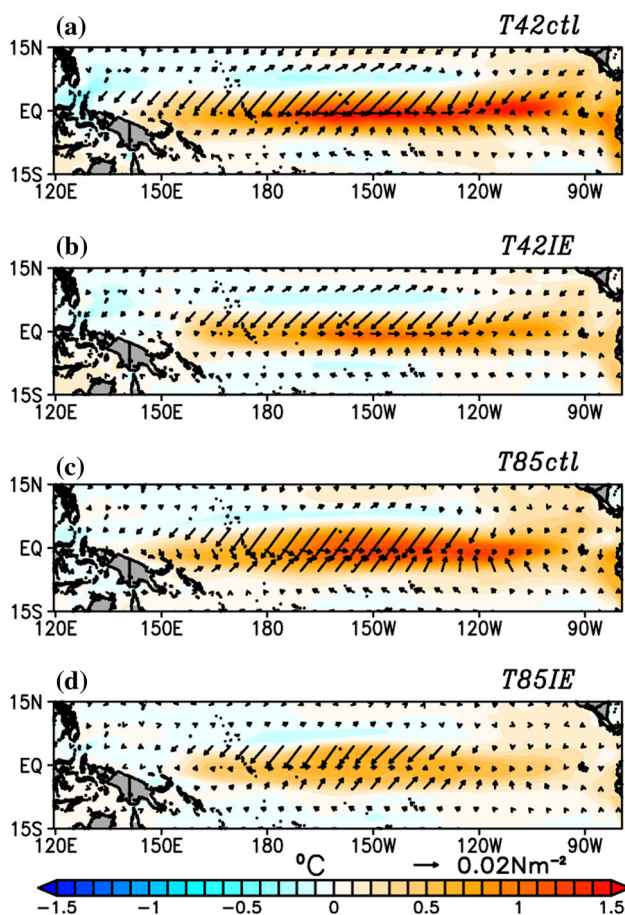


Fig. 7 ENSO linear (symmetric) responses for sea surface temperature anomaly SSTA (shaded, $^{\circ}\text{C}$) and surface wind stress (vector, Nm^{-2}). The linear ENSO response is defined by subtracting the warm events composite to the cold events composite and dividing by 2 due to opposite polarity. The composite for both ENSO phases includes over 30 events, defined by magnitudes greater than one Niño3.4 SSTA standard deviation. **a** Corresponds to T42ctl, **b** to T42 IE, **c** to T85ctl, and **d** to T85 IE respectively

symmetric part is then, divided by 2. For each experiments, there are over 40 warm and cold events contributing to the composites. Figures 7 and 8 show the symmetric and asymmetric ENSO response respectively for T42ctl (a), T42 IE (b), T85ctl (c), and T85 IE (d) respectively. SSTAs [$^{\circ}\text{C}$] are depicted by shaded contours and wind stress [Nm^{-2}] by vector contours.

5.3.1 Low (T42) resolution

For T42ctl (Fig. 7a), the symmetric component of ENSO has SSTA that is narrowly confined to the equator, with higher amplitudes in the central basin and significant equatorial wind stress convergence over most of the positive SSTA region. Overall, almost all the symmetric ENSO signal is confined to a narrow band from 10°S to 10°N . The asymmetric ENSO component is shown in Fig. 8a for

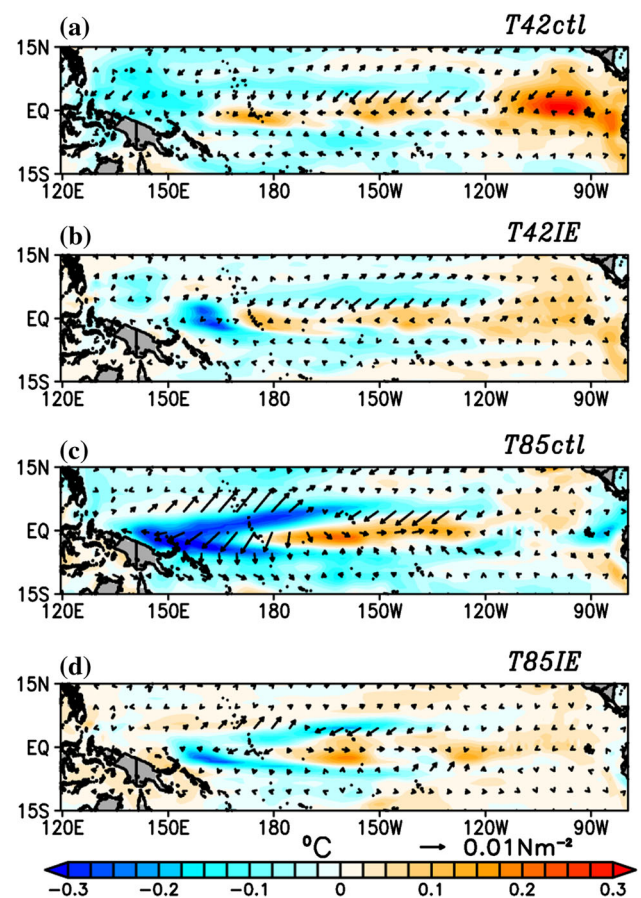


Fig. 8 Same as 7, but for the ENSO non-linear (asymmetric) response. The asymmetric or phase-asymmetry is defined by adding the warm to the cold event composite. **a** Corresponds to T42ctl, **b** to T42 IE, **c** to T85ctl, and **d** to T85 IE respectively

T42ctl. Note the difference in contour interval with respect to Fig. 7 indicating that the asymmetric component is on the order of 25 % of the symmetric component. The positive center of action off the coast of South America in SST (Fig. 8a) suggests that the warm phase has larger amplitude there. This is consistent with observational estimates (Chiang and Vimont 2004). Generally speaking, the cold phase dominates throughout most of the domain, especially over the western portion of the basin. Unlike for the symmetric component, there is some off-equatorial activity in the wind stress and SST.

Similarly, Figs. 7b and 8b depicts the symmetric and asymmetric ENSO response in T42 IE. There is a clear reduction in amplitude (about 20 %) for the symmetric response in IE. The overall spatial coherence is unchanged for the SST and wind stress. Perhaps, the biggest difference is in the reduced western extent of the SST. For the IE experiment, the eastward shift could be associated with the slight cooling of SSTs over the western Pacific shown earlier. For the asymmetric response (Fig. 8b), the warm SST center of action off the coast of Peru weakens

significantly, suggesting that whatever is responsible for it is related to the weather noise forcing. As with T42ctl, most of the asymmetry is negative, especially in the western Pacific and just off the equator. Most of the phase asymmetry beyond 10° north and south weakens but what variability remains lies within the 10°S – 10°N latitudinal bands. This argues that most of the noise reduction is away from the equator, or at least, noise has a greater relative effect there.

5.3.2 Medium (T85) resolution

The same analysis is repeated using the T85 simulations. Again, more than 40 warm and cold events contribute to the composite for both control and IE experiments. Before comparing the effect of the IE technique, we first describe difference in the control runs (Figs. 7a, c, 8a, c). For the symmetric response (Fig. 7a, c), the amplitude of the symmetric signal is reduced in the east in T85, and a slight reduction in the west. The more marked differences are in the asymmetric response (Fig. 8a vs. c). Here, it is clearly shown that at higher resolution, the ENSO phase asymmetry increases significantly, and the structure sharpens dramatically. This sharper structure is most apparent in the western Pacific where the T85 model has a well-defined sideways cold “v” pattern that is blurred and even difficult to detect in the T42 model. The warm signal in the center of the “v” is also more clearly defined in the T85 model. The strong warm asymmetric signal seen in T42ctl (Fig. 8a) is completely removed and even weakly negative in T85ctl.

Figures 7d and 8d demonstrate the symmetric and asymmetric ENSO response for T85 IE experiment. For the symmetric response, the amplitude of anomalies is significantly smaller as compared to T85ctl. In fact, variance drops by about 50 %, this is considerably larger drop than at T42 resolution. Most of the symmetric response is located over the central basin and in a narrow equatorial latitudinal band. When looking at the phase asymmetry, the overall reduction in amplitude is consistent in the two resolution IE experiments. The most marked reduction at T85 is the cold sideways “v” pattern in the western Pacific. This is a region where the T85ctl simulation has considerable rainfall variability that is apparently associated with asymmetric SSTA variability that is not captured at T42, and that is significantly reduce when the IE coupling is applied. We should also note that this is a region where CCSM3 has particular difficulty in capturing the mean structure of the SST (see Fig. 1) and rainfall, and is the region where the IE apparently improves the overall structure of the western Pacific warm pool plateau (see Fig 1).

The ENSO phase asymmetry while different at different resolutions is clearly dependent on the noise. However, it is not clear whether the changes in the symmetric and

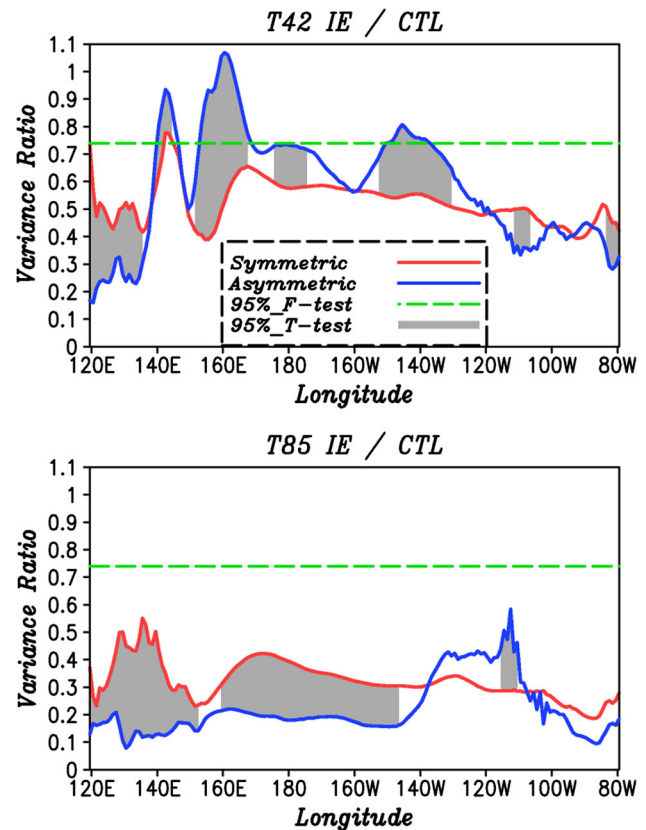


Fig. 9 Ratio of IE versus control experiments (T42 top) and (T85 bottom) for symmetric (red) and asymmetric (blue) components calculated as a variance using the SSTA composite squared across the equatorial Pacific. The components are meridionally averaged from 10°S to 10°N . The horizontal dashed-green line corresponds to variance ratios significance to a 95 % confidence level based on F-test. Regions depicted by grey shade indicate where the phase asymmetry (e.g. warm plus cold) are different than the phase symmetry to a 95 % confidence level based on a Student *T* test

asymmetric component are simply associated with the overall variance reduction or whether there are some asymmetric effects due to the noise reduction. Simply put, is the observed reduction in asymmetry due to noise or is it a result of significant amplitude reduction in the symmetric component?

To address the above question, Fig. 9 describes the ratio of IE versus control experiments and for symmetric (red) and asymmetric (blue) components calculated as a variance using the SSTA composite squared across the equatorial Pacific. The components are meridionally averaged from 10°S to 10°N . There are two diagnostic elements evaluated in Fig. 9:

- (i) *Impact of noise reduction separately for the symmetric and asymmetric components evaluated across atmospheric model resolution.* The horizontal dashed-green line corresponds to variance reductions that are significance to a 95 % confidence level based on F-test. Essentially, if the blue and/or red

lines are below the green dashed line, then the IE coupling significantly reduces the variance of the symmetric component in the case of the red line and/or the asymmetric component in the case of the blue line. If the red or blue are above the green, then the variance reductions fail to be significant according to this F test. The larger variance reduction at T85 is readily apparent, and perhaps more interesting is that the variance reduction is larger for the asymmetric component. This can be seen by the fact that the blue line in the top panel generally lies above the red, and generally lies below the red in the bottom panel. Indeed, there are large regions where the T42 asymmetric component is not significantly reduced in the IE simulation, whereas in the T85 case the red and blue lines are well separated from the 95 % confidence line.

- (ii) *Impact of noise reduction on symmetric and asymmetric components within a specific resolution.* Regions depicted by grey shading indicate where the IE effect on phase asymmetry (e.g. warm plus cold) is different than the IE effect on phase symmetry to a 95 % confidence level based on a Student T test for a particular resolution. In other words, if the IE effect was the same for the symmetric and asymmetric components of say the T42 model, then the red and blue curves in the top panel would be statistically indistinguishable. The same argument applies for the T85 case. For T42 resolution, the effect of noise reduction on the asymmetric component is smaller than that on the symmetric component that is statistically significant for fairly large regions of the central Pacific. In the west Pacific, at T42 the IE effect is larger for the asymmetric component. In the east Pacific the reduction is similar for both the symmetric and asymmetric components. At T85, throughout much of the west and central Pacific the IE effect is significantly larger to the asymmetric component.

There are some final points to note with Fig. 9. For example, the positive center of action off the coast of South America in the T42 model (Fig. 8a) is reduced by a similar amount both the symmetric and asymmetric component, therefore we conclude that this reduction is due to the overall reduction in variance and is not specific to ENSO asymmetry. At T85 (Fig. 9 bottom), the asymmetry is strongly degraded (i.e., ~ 0.2 or 20 %) and is significantly different than the symmetric effect for most of the central and eastern Pacific. Recall from Fig. 8c, d that these are the regions of largest differences in phase showing the cold sideways “v” pattern.

The marked reductions in amplitude over both symmetric and asymmetric ENSO characteristics further

highlight the importance of weather noise in ENSO dynamics. More interestingly, the importance of the noise appears to increase with resolution. This resolution dependence is clearly shown in the asymmetric component plots, where T85ctl is the most asymmetric simulation and T85 IE is the least asymmetric of all the experiments. Also, the marked reduction in asymmetry at T85 appears to be different than just a reduction in the amplitude of the symmetric component. That is, much of the asymmetry at T85 is noise driven.

5.3.3 Asymmetry due to noise

The source of the asymmetry is an ongoing debate in the ENSO community. Timmermann et al. (2003) proposed a non-linear bursting scenario for extreme warm events. Differences in amplitude between El Niño and La Niña phase could be attributed to non-linear dynamical thermal advection (Jin et al. 2003). Kang and Kug (2002) suggested that atmospheric non-linear response to warm and cold SSTA could lead to ENSO phase asymmetry. Thus far, the results presented here suggest that at least some of the asymmetry is due to atmospheric internal dynamics or noise at the air-sea interface. There are at least two possible mechanistic explanations for how the noise supports asymmetry: (i) that the noise is different for warm versus cold events (i.e., non-linearity in the noise forcing itself), or (ii) that warm and cold events respond differently to the same noise (i.e., non-linearity in the response to the noise forcing).

We consider here (i) above, that is the possibility that the noise is different for warm and cold events. In order to examine the potential for non-linearity in the response to the noise forcing (i.e., ii above), additional experiments may be required which are beyond the scope of this study.

To address the first possibility—namely that the noise statistics are different for warm and cold events we examine the wind stress noise separately for warm and cold events. One of the advantages of the IE technique is that there are six atmospheric realizations that are responding to the same ocean forcing. Therefore, it is possible to quantify atmospheric internal variability by simply analyzing the ensemble spread among the atmospheric simulations. Here, we define the ensemble spread based on all possible differences among the ensemble members, this yields $M = 15$ different combinations.

$$\text{Ensemble spread} = \left[\frac{1}{M} \sum_{i=1}^M (x_i - x_{i+1})^2 \right]^{1/2} \quad (1)$$

Equation (1) is suitable for our IE cases where multiple atmospheric simulations are readily available. Given that our control simulations only contain one atmosphere

coupled to one ocean, (1) cannot be used for extracting the atmospheric noise. For the control simulation, we attempt to extract the noise using the following procedure. First, a given variable $x^k(t)$ can be decomposed by a linear signal $Ln(t)$, a non-linear signal $NL(t)$, and noise as described in (2). Here, k represents the ensemble member, which for control case is just $x(t)$ since there is only one ensemble member. For our case, variable $x(t)$ is zonal wind stress. The linear signal is just modeled by a simple linear regression between Niño3.4 SSTA and variable $x(t)$. A remainder $R(t)$ can be obtained by subtracting the linear signal from the total field $x(t)$, so that $R(t)$ includes the non-linear signal plus the noise component only. Here, we refer to $NL(t)$ as the component of the signal that is not extracted by the linear regression. In order to separate the noise in the remainder, we make use of composite averaging as in (3). The $\overline{R(t)}$ term inside the square bracket in (3) denotes the composite averaging for N warm or cold events. If N is large enough, $\overline{R(t)}$ should mostly contain the non-linear signal associated with those N events. Finally, a spread or noise can be obtained by the root-mean-square difference between the residual $R(t)$ and $\overline{R(t)}$. It should be noted that event-to-event variations in the ENSO asymmetry could be included in the noise estimate $R_i(t)$.

$$x^k(t) = Ln(t) + NL(t) + Noise^k(t) \quad (2)$$

$$Noise(t) = \left[\frac{1}{N} \sum_{i=1}^N \left(R_i(t) - \overline{R(t)} \right)^2 \right]^{1/2} \quad (3)$$

Given both the control and the IE simulations we can test whether (1) and (3) provide similar noise estimates. Figure 10 depicts equatorial Pacific Hovmöller diagrams of zonal wind stress noise evolution averaged over all warm (El Niño) events. Panels (a) and (d) correspond to T42 IE and T85 IE noise structure calculated using Eq. (1). Similarly, panels (b) and (e) correspond to T42 IE and T85 IE noise structure using Eq. (3). Panels (c) and (f) are similar to (b) and (e) respectively but Eq. (3) is applied to the ensemble mean of $x^k(t)$ ($N = 6$ for IE cases) wind stress given that that is what forces the ocean model. The first point to make here is that both definitions of noise (i.e., Eqs. 1 and 3) produce similar noise estimates. This can be seen by the fact that Fig. 10a is very similar to Fig. 10b, d is very similar to Fig. 10e. Results from (3) have slightly less localized amplitude than those from (1) but the general structure in evolution corresponds well. Based on Fig. 10 we assert (3) is a reasonable estimate of the noise evolution and can be used to compare noise in the control with IE where only one atmosphere simulation is readily available.

The second point to make with Fig. 10 is that the noise is considerably smaller when Eq. (3) is applied to the ensemble mean of $x^k(t)$. This is expected and is

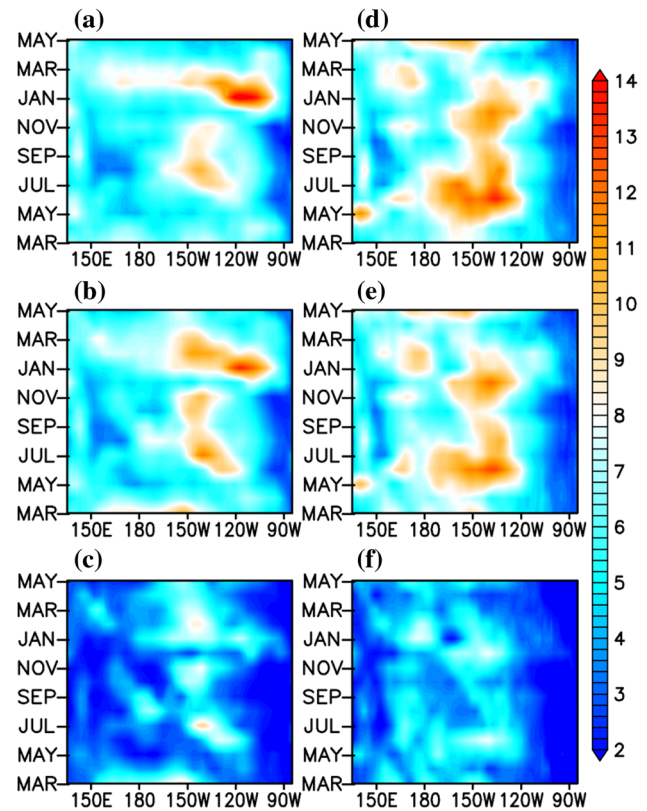


Fig. 10 Hovmöller diagram depicting zonal wind stress [10^{-3}Nm^{-2}] noise evolution across the equatorial Pacific during warm (El Niño) events. **a, d** correspond to T42 IE and T85 IE noise calculated using Eq. (1), where **b** and **e** correspond to T42 IE and T85 IE noise using Eq. (3). **c, f** Similar to **b, e** respectively but Eq. (3) is applied to the ensemble mean ($N = 6$ for IE cases) wind stress given that that is what forces the ocean model. The *horizontal axis* corresponds to longitude across the equatorial Pacific Ocean. The *vertical axis* corresponds to lead-time in months. Composite is based on Niño3.4 sea surface temperature anomaly (SSTA) centered during December–January–February

highlighting how the IE technique works. The noise in panels (b) and (e) can be thought as atmospheric internal dynamics (AID) for a particular atmosphere ensemble member indicating that individual IE ensemble members can be used to estimate noise in the control, whereas panels (c) and (f) are the actual wind stress noise forcing to the ocean when the IE technique is applied. It should also be mentioned that all individual ensemble members show a similar noise pattern.

Figure 11 shows the evolution of the noise for zonal wind stress for warm and cold events for all four simulations. For the control simulations, noise evolution between warm and cold events is fundamentally different. For example, for the T42ctl case, the cold phase appears to have larger noise amplitude during the growth phase (e.g., from May to November) than that of the growth phase of warm events. In contrast, there is larger noise amplitude for

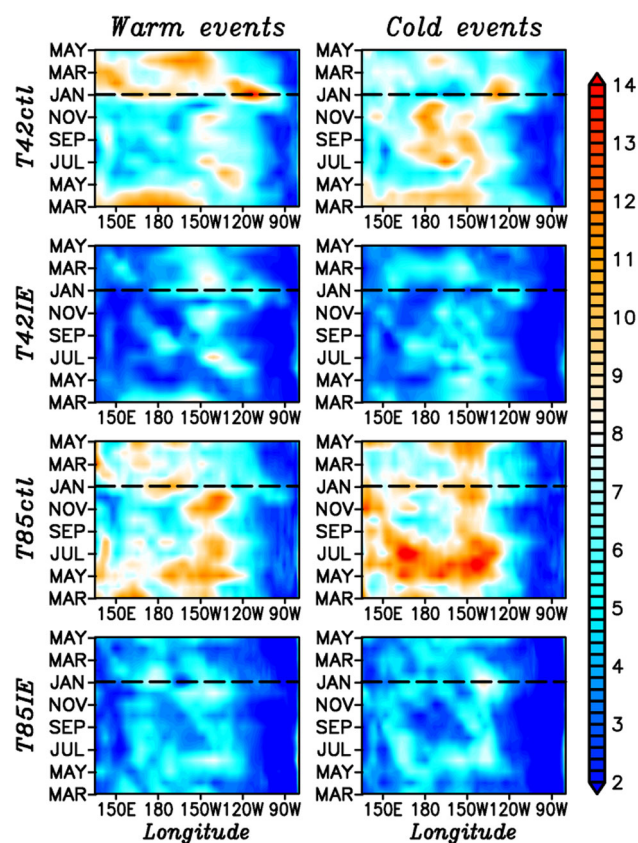


Fig. 11 Hovmöller diagram depicting zonal wind stress [10^{-3} Nm^{-2}] noise evolution across the equatorial Pacific during warm (El Niño) events (left column) and during cold (La Niña) events (right column) for each experiment (rows). The horizontal axis corresponds to longitude across the equatorial Pacific Ocean. The vertical axis correspond to lead time in months, where year (0) is prior and year (1) is post the peak event. Composite is based on Niño3.4 sea surface temperature anomaly (SSTA) with horizontal black-dashed line representing zero-lag centered during December–January–February. The noise is defined by Eq. (3) applied to the ensemble mean ($N = 1$ for control and $N = 6$ for IE cases) wind stress given that that is what forces the ocean model

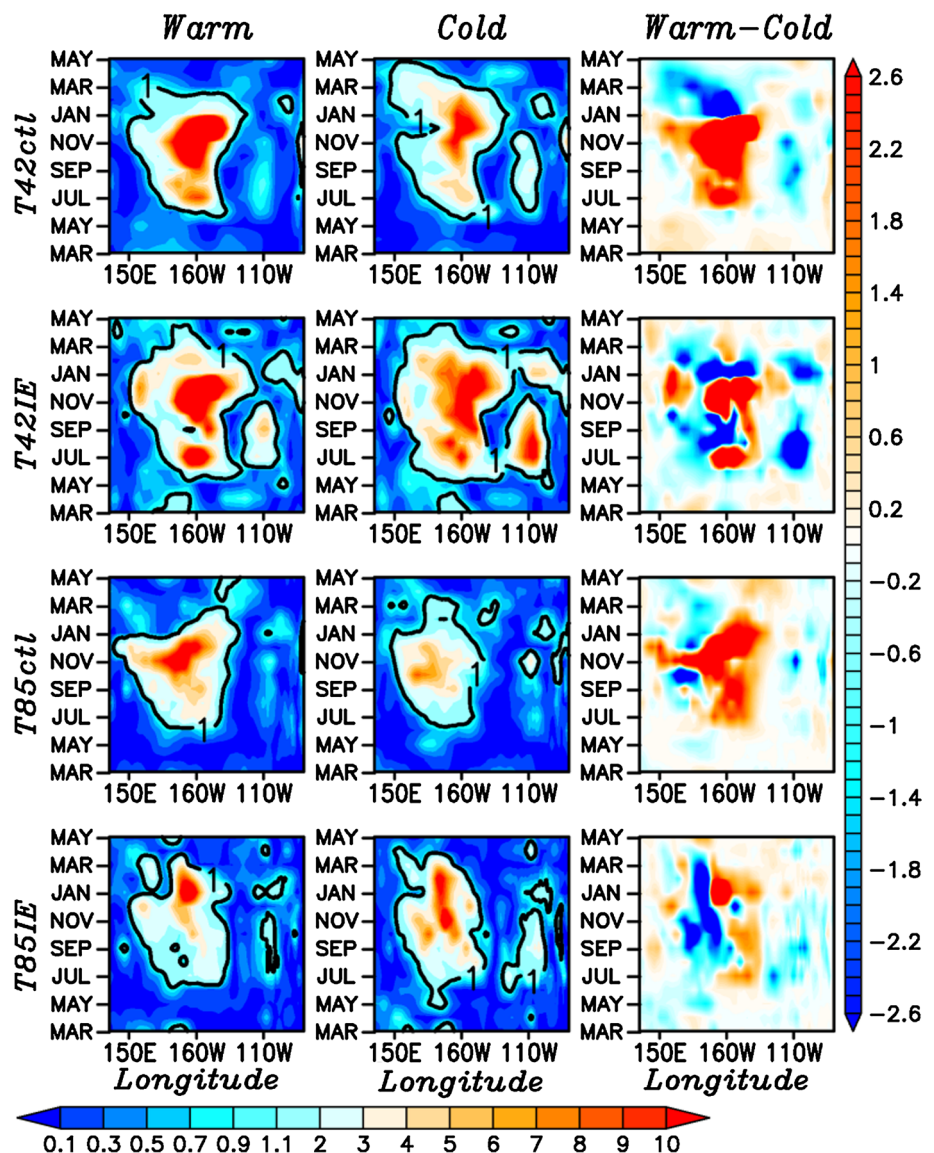
warm events during the maximum SSTA. Similarly, the T85ctl case has the largest noise for the La Niña phase with a late spring maxima. Recall that this is the season of very significant cold SSTA spread (see Fig. 6 T85ctl panel). Also, Fig. 4 shows more late boreal spring variance in T85ctl compared to T42ctl, where T85 IE variance is consistently smaller than T42 IE throughout the year. This suggests that the enhanced SSTA variance in T85ctl (Fig. 4) during late spring is highly noise induced. The noise asymmetry is largely reduced for the IE cases. The T42 IE model has some apparent phase dependence and any phase dependence in the T85 IE simulation is difficult to detect at best. The bottom line is that the phase asymmetry in both the SSTA evolution and the noise statistics is clobbered by applying the IE coupling.

Given that the noise amplitude may depend on the signal amplitude, we cannot definitively determine from Fig. 11 whether the noise is larger in T85 or T42. We can address this to some extent by considering the signal-to-noise ratio where the noise is defined by (3) for all cases. Figure 12 shows the zonal wind stress signal-to-noise ratio evolution (shaded) during warm ENSO events (left-column), similarly for cold events (middle-column). Differences in warm minus cold signal-to-noise ratio are shown (right-column). The signal is defined as the absolute value of the ensemble mean anomaly. Recall that the signal in the control runs is defined by compositing several events, but each event only has a single realization. In contrast, for the IE runs, the signal is defined by composite of the ensemble mean of multiple realizations for several events. For all cases, the highest signal-to-noise ratios are observed over the central Pacific, and this is mostly over the maximum SSTA variance region. Consistent with Fig. 11, warm events are less noisy than cold events for the control simulations. Interesting, the higher resolution case depicts significantly smaller signal-to-noise ratios compared to the low-resolution case, suggesting that T85 has more noise than T42 relative to the signal amplitude. This is especially true for cold events. Moreover, the warm-cold asymmetry in the signal-to-noise ratio is larger in amplitude and has a more coherent structure for both control cases with respect to the IE cases. This simply means there is less phase asymmetry in the IE simulations.

This study concentrates on internal atmospheric dynamics and coupled processes over the tropical Pacific only. However, it is useful to examine some of the basic characteristics of internal atmosphere variability in the extratropics that may play a role in diversifying ENSO events. For this, we computed Empirical Orthogonal Functions (EOF) of the internal atmosphere variability as defined in Eq. (3). Here, the EOF analysis is applied to the March–April–May (MAM) sensible heat flux and latent heat flux during El Niño and La Niña events. These events are defined based on the Niño3.4 standard deviation. The internal atmosphere variability is defined as the deviation from the ensemble mean of all events. For example, the T42ctl case has only one atmospheric realization but over 60 warm and 60 cold events. This gives over 60 maps of the internal atmospheric variability for which we calculate the EOF. On the other hand, the T42 IE case has 6 ensemble members and about 50 warm and cold events. This gives 6×50 or 300 maps of internal atmospheric variability for EOF analysis.

The motivation for analyzing atmospheric noise in terms of boreal spring latent and sensible heat fluxes over the North Pacific is as follows. The work of Vimont et al. (2003a, b) identified a mechanism by which mid-latitude atmospheric variability influences ENSO, namely the

Fig. 12 Zonal wind stress signal-to-noise ratio evolution across the equatorial Pacific during warm ENSO events (*left-column*), similarly for cold events (*middle-column*). *Black contours* show where the signal-to-noise ratio equals unity. Differences in warm minus cold signal-to-noise ratio are shown (*right-column*) with *black contours* depicting differences equals 0.5. Composite is based on Niño3.4 sea surface temperature anomaly (SSTA) centered during December–January–February



“seasonal foot-print mechanism.” The process is that mid-latitude internal atmospheric variability during winter imparts an SST “footprint” through modification of the surface heat fluxes. This SST footprint persists through the boreal spring season with associated heat fluxes and atmospheric circulation anomalies. Vimont et al. (2003a, b) also noted that the seasonal footprint mechanism is not the primary ENSO mechanism but means for stochastic forcing of ENSO. The spatial structure of this mechanism closely resembles the so-called North Pacific Oscillator of Rogers (1981) and was also detected as an ENSO precursor in CCSM4 (Larson and Kirtman 2013).

Figure 13 depicts the spatial structure of the leading EOF of latent and sensible heat flux. The latent heat flux is one order of magnitude larger than sensible heat flux for all cases. The spatial structure of atmospheric internal variability in Fig. 13 strongly resembles that associated with

the seasonal footprint mechanism discussed earlier (Vimont et al. 2003a, b). The noise asymmetry seen in the control cases (e.g., T42ctl and T85ctl) nearly vanishes in the noise-reduced experiment (e.g., T42 IE and T85 IE). This result is more pronounced for the T85 resolution case. Internal atmospheric variability is significantly asymmetric in amplitude and structure for T85ctl, but nearly identical for T85 IE case. These results support those presented in the original manuscript in that atmospheric variability is asymmetric, both in the tropics and mid-latitude. This leads to asymmetric ENSO forcing that ultimately leads to an asymmetric ENSO response.

Thus far, we have demonstrated that atmospheric noise is fundamental in sustaining ENSO variability and asymmetry, particularly as the resolution increases. What has not been clarified is that if the relative structure of the noise with respect to the signal is responsible for the marked

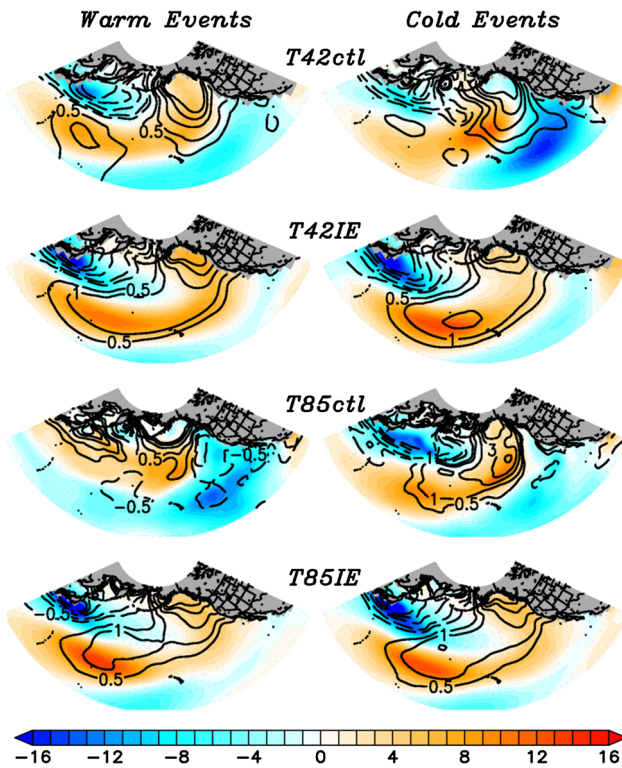


Fig. 13 Spatial structure of the leading structure (i.e., EOF1) of the internal atmosphere variability of latent (sensible) heat flux shown by shaded (black contour) in Wm^{-2} for the North Pacific during March–April–May leading to warm (left) and cold (right) ENSO events. These events are defined based on the Niño3.4 standard deviation. The internal atmosphere variability is defined as the deviation from the ensemble mean of all events

resolution dependence in these results. That is, as resolution increases the dominant noise structure start to deviate from the dominant signal patterns. Recall that Kirtman et al. (2005) with a T42 model argued that the noise and signal spatial structures were similar, and that we hypothesized here that this was the case with the T42 case, but not T85. To test this hypothesis, we compare the noise structure presented in Fig. 11 with the signal structure. We remind the reader that the noise is calculated using (3) and the signal is defined as the ensemble mean for all events,

Figure 14 describes the zonal wind stress [10^{-3}Nm^{-2}] structure across the equator for the (a) T42 and (b) T85 models for warm and cold events combined. Thick-dashed lines depict the signal and thick-solid lines depict the noise for the control (black) and IE (grey). Atmosphere internal dynamics (AID) is determined by applying (3) to each individual IE ensemble member and is indicated by thin-dotted lines. All fields are meridionally averaged from 2°N to 2°S . Note that for the two control cases (i.e., T42ctl and T85ctl) the AID and noise is the same as there is only one atmosphere for these cases. Alternatively, the noise felt by the ocean component in the IE simulations (thick solid grey

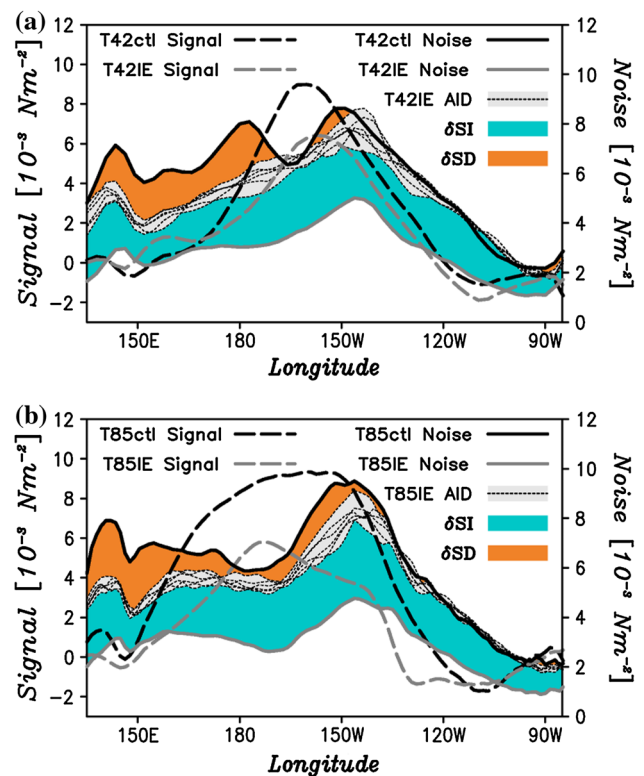


Fig. 14 Zonal wind stress [10^{-3}Nm^{-2}] structure a cross the equator for; **a** T42 and **b** T85 resolution model for warm and cold events combined. Thick-dashed lines depict the signal and thick-solid lines depict the noise for control (black) and IE (grey) experiment. Atmosphere internal dynamics (AID) for each IE ensemble member is shown by thin-dotted lines. Signal-independent noise reduction (δSI) is highlighted by light-blue shade, whereas signal-dependent noise reduction (δSD) is shown by orange shade. All fields are meridionally averaged from 2°N to 2°S

line) is calculated by applying (3) to the ensemble mean wind stress. The curves denoted as noise are the standard deviation, and hence are positive definite (see y-axis on the right). The signal fields include the sign dependence (see y-axis on the left). It is important to note that the signal and noise structure are separately calculated for warm and cold events before they are combined.

In Fig. 14, the signal-independent noise reduction (δSI , light blue shade) can be estimated as the difference between the thin grey dashed curves and the thick solid grey curve. This is because the noise standard deviation in the individual ensemble members (thin grey dashed curves) and the noise standard deviation in the ensemble mean (thick solid grey curve) are calculated from the same IE simulation where all atmospheric ensemble members feel the same SST (i.e., same signal). The atmospheric ensemble members have the same signal; therefore, the differences noted in Fig. 14 are the signal independent noise reduction. Alternatively, the signal dependent noise differences (δSD , orange shade) can be estimated by

comparing the control noise standard deviation with the noise standard deviation of each individual ensemble member in the IE simulation. Here we are assuming that the individual IE ensemble member would have the same noise standard deviation as the control if the IE SST was the same as the control SST. Of course, the control SST and IE SST have very different signals, and therefore the differences in the noise standard deviations are assumed to be signal dependent noise—at least in the sense of the overall amplitude.

A few important points to note with Fig. 14:

- The amplitude reduction in the zonal wind stress signal is significantly larger at T85 (compare grey dashed with black dashed), consistent with reduction in SSTA signal.
- The zonal structure of the wind stress signal is more similar to the noise structure at lower (T42) resolution. This can be seen by noting the noise in the T42 simulation is more peaked in the central Pacific where the signal also peaks. At T85 the noise amplitude has a minimum where the signal has a peak in the central Pacific. This is also consistent with Fig. 3 in that the spatial structure of variance ratio (σ_{IE}/σ_{CTL}) resembles the spatial structure of the control (σ_{CTL}) at T42 but is different at T85.
- There is little changes in the amplitude of the noise due to changes in the signal (δSD) east of 150°W suggesting that most of the noise over the cold-tongue region is state independent. The largest δSD are west of 150°W suggesting that most of the state dependent noise occurs over the warm-pool region. This is independent on model resolution only that at T85 the δSD extends further east.

6 Summary and discussion

A state-of-the-art climate system model, namely CCSM3, was adopted in order to study the effect of weather noise and its resolution on tropical Pacific variability. For this, four different experiments were compared. In particular, two control experiments were presented at different resolutions, a low resolution $\sim 2.8^\circ$ and a medium resolution $\sim 1.4^\circ$ grid spacing for the atmospheric component (see Deser et al. 2006 of these simulation). Note that the ocean model resolution is the same for all cases. Two additional experiments were performed at these resolutions where the impact of internal atmospheric dynamics was suppressed by a noise reduction technique. The noise reduction technique adopted is the interactive ensemble approach from Kirtman and Shukla (2002) where ensemble averages of multiple AGCM realizations are coupled to a single OGCM as the model evolves.

Over the tropical Pacific Ocean, the noise reduction has significant impacts almost everywhere in both the mean and the variability. These changes include increased cold bias over the eastern Pacific, closer to observed SST simulation over the warm pool including, the appearance of a SST plateau west of 160°E longitude, an observed feature that is not simulated on the control simulations. One of the systematic errors of this model is the warmer than observed SST off the South American coast, this is also reduced by the noise reduction. It is possible that the model has too much noise forcing over regions where the noise-reduced simulations are in better agreement with the observational estimates. These results are more marked with the higher resolution case. This also possibly suggests that at coarser resolution, the noise is so large scale that the IE technique is interpreting it as signal. The improvements noted above should not be interpreted as an argument for using the IE technique for direct model improvement. This is merely a diagnostic that suggests that the AGCM noise may be too strong in these particular regions.

We analyzed the variability of SST, zonal wind stress, and precipitation anomalies. At higher resolution, there is a 10 to 30 % more variance reduction when compared to the low-resolution case. Variance ratios between IE and control cases suggest that noise is more important in forcing tropical Pacific variability as resolution increases. In the higher resolution case the Niño3.4 standard deviation is reduced by $\sim 60\%$. From both resolutions, noise appears to play no role in the ENSO period, at least for this particular model. ENSO phase locking to the annual cycle is also modified by noise reduction. The two control simulations have distinct differences during the boreal spring season. This difference is eliminated in the noise-reduced simulations.

The ENSO evolution during the calendar year was very distinct between the two models. In the T85 simulations, the SSTA emerges about two months earlier (e.g., early April) than those from the low-resolution model (e.g., late May). This difference appears to be related to a difference in the noise evolution, with the T85 model having significantly stronger noise forcing during the boreal spring.

The irregularity among ENSO events was studied using two different approaches. First, we separately quantified differences among warm events and differences among cold events. That is, we compute the spread of El Niño and La Niña events separately with and without the presence of noise. It was observed that both control simulations depicted similar and significant spread for warm events. Reducing the noise reduces the spread of events, especially for the higher resolution case where there was very little differences among the warm events. For the cold phase, the higher resolution control model shows the most irregularity

among all the experiments, and the high resolution IE had the smallest differences among the individual events—again pointing to the fact that atmospheric noise is more important at high resolution. This irregularity is strongest during late boreal spring, which corresponded to significantly larger zonal wind stress noise forcing. This suggests that most of the event-to-event differences are driven by atmospheric noise as opposed to chaotic dynamics within the context of the large-scale coupled system. Moreover, this also suggests that there is a well-defined “canonical” event in this coupled model.

ENSO phase asymmetry was also examined. We acknowledge the weak asymmetry in CCSM3 compared to observations as pointed by Zhang et al. (2009a). However, in this paper, we were able to show that ENSO asymmetry in this model is still statistically significant. More importantly, the asymmetry is significantly reduced when atmospheric noise is reduced via Interactive Ensemble coupling. The higher resolution control has the most asymmetry, and the higher resolution noise-reduced IE case has the least asymmetry. That is, applying the noise reduction technique had the largest impact in reducing the asymmetry of ENSO at T85 resolution. It was found that the ENSO phase asymmetry is strongly related to the noise forcing. This supports the argument (at least in this model) that the “canonical” warm and cold events are linear and that the observed asymmetry is either associated with differences in the space–time structure of the noise (i.e., non-linearity in the noise) or in the response to the noise (i.e., non-linearity in the response). While we did not examine the non-linearity in the response to the noise, we did demonstrate that noise itself is asymmetric, with larger spread in the zonal wind stress during La Niña events. This result was further validated by analysis of the noise structure in the extratropics.

Analysis on the zonal wind stress across the tropical Pacific suggested that the spatial structure of the noise starts to deviate from the signal as resolution increases. We separated the state independent and state dependent noise amplitude, and found that the atmospheric noise in the eastern Pacific was largely state independent. In contrast, most of the reduction in the amplitude of noise in the western Pacific was state-dependent.

Certainly, these results should be tested with even higher resolution atmospheric models and different coupled systems. Of course issues related to ocean resolution should also be investigated. Nevertheless, the results suggest that many properties of ENSO statistics (amplitude, phase locking with the annual cycle, phase asymmetry) are resolution dependent. This raises important question regarding how well do we need to resolve weather statistics in order to capture the correct mechanisms for climate variability.

Acknowledgments This manuscript is part of a Ph.D dissertation of the first author. The first author would like to express thanks to Prof. Chidong Zhang (RSMAS, U. of Miami), Prof. Mohamed Iskandarani (RSMAS, U. of Miami), Prof. Robert Burgman (Florida International University). We are grateful to the reviewers for their suggestions. The authors acknowledge support from NSF ATM0754341, OCI10749165 and NOAA NA08OAR4320889.

References

- Blanke B, Neelin JD, Gutzler D (1997) Estimating the effect of stochastic wind stress forcing on ENSO irregularity. *J Clim* 10:1473–1487
- Chang PB, Zhang L, Saravanan R, Vimont D, Chiang JCH, Ji L, Seidel H, Tippett MK (2007a) Pacific meridional mode and El Niño–Southern Oscillation. *Geophys Res Lett* 34:L16608. doi:[10.1029/2007GL030302](https://doi.org/10.1029/2007GL030302)
- Chang P, Zhang L, Saravanan R, Vimont DJ, Chiang JCH, Ji L, Seidel H, Tippett MK (2007b) Pacific meridional mode and El Niño—Southern Oscillation. *Geophys Res Lett* 34:L16608. doi:[10.1029/2007GL030302](https://doi.org/10.1029/2007GL030302)
- Chen SS, Houze RA Jr, Mapes BE (1996) Multiscale variability of deep convection in relation to large-scale circulation in TOGA COARE. *J Atmos Sci* 53:1380–1409
- Chen Y-Q, Battisti DS, Palmer TN, Barsugli J, Sarachik ES (1997) A study of the predictability of tropical Pacific SST in a coupled atmosphere–ocean model using singular vector analysis: the role of the annual cycle and the ENSO cycle. *Mon Wea Rev* 125:831–845
- Chiang J, Vimont D (2004) Analogous Pacific and Atlantic meridional modes of tropical atmosphere–ocean variability. *J Clim* 17:4143–4158
- Chu P-S (1988) Extratropical forcing and the burst of equatorial westerlies in the western Pacific: a synoptic study. *J Meteor Soc Jpn* 66:549–563
- Collins WD et al (2006) The Community Climate System Model version 3 (CCSM3). *J Clim* 19:2122–2143
- Deser C, Capotondi A, Saravanan R, Phillips A (2006) Tropical Pacific and Atlantic variability in CCSM3. *J Clim* 19:2451–2481
- Eckert C, Latif M (1997) Predictability of a stochastically forced hybrid coupled model of El Niño. *J Clim* 10:1488–1504
- Flügel M, Chang P (1996) Impact of dynamical and stochastic processes on the predictability of ENSO. *Geophys Res Lett* 23:2089–2092
- Flügel M, Chang P, Penland C (2004) The role of stochastic forcing in modulating ENSO predictability. *J Clim* 17:3125–3140
- Jin F-F, An S-I, Timmermann A, Zhao J (2003) Strong El Niño events and nonlinear dynamical heating. *Geophys Res Lett* 30:1120. doi:[10.1029/2002GL016356](https://doi.org/10.1029/2002GL016356)
- Jin F-F, Lin L, Timmermann A, Zhao J (2007) Ensemble-mean dynamics of the ENSO recharge oscillator under state-dependent stochastic forcing. *Geophys Res Lett* 34:L03807. doi:[10.1029/2006GL027372](https://doi.org/10.1029/2006GL027372)
- Kang I-S, Kug J-S (2002) El Niño and La Niña sea surface temperature anomalies: asymmetric characteristics associated with their wind stress anomalies. *J Geophys Res* 107(D19):4372–4381
- Keen RA (1982) The role of cross-equatorial tropical cyclone pairs in the Southern Oscillation. *Mon Wea Rev* 110:1405–1416
- Kiladis GN, Meehl GA, Weickmann KM (1994) Large-scale circulation associated with westerly wind bursts and deep convection over the western equatorial Pacific. *J Geo Phys Res* 99:18527–18544

- Kirtman BP (1997) Oceanic Rossby wave dynamics and the ENSO period in a coupled model. *J Clim* 10:1690–1704
- Kirtman BP, Min D (2009) Multimodel ensemble ENSO prediction with CCSM and CFS. *Mon Wea Rev* 137:2908–2930
- Kirtman BP, Schopf PS (1998) Decadal variability in ENSO predictability and prediction. *J Clim* 11:2804–2822
- Kirtman BP, Shukla J (2000) Influence of the Indian summer monsoon on ENSO. *Quart J Roy Meteor Soc* 126:213–239
- Kirtman BP, Shukla J (2002) Interactive coupled ensemble: a new coupling strategy for GCMs. *Geophys Res Lett* 29:1029–1032
- Kirtman BP, Fan Y, Schneider EK (2002) The COLA global coupled and anomaly coupled ocean-atmosphere GCM. *J Clim* 15:2301–2320
- Kirtman BP, Pegion K, Kinter S (2005) Internal atmospheric dynamics and climate variability. *J Atmos Sci* 62:2220–2233
- Kirtman BP, Straus DM, Min DH, Schneider EK, Siqueira L (2009) Toward linking weather and climate in the interactive ensemble NCAR climate model. *Geophys Res Lett* 36
- Kirtman BP, Schneider EK, Straus DM, Min D, Burgman R (2011) How weather impacts the forced climate response. *Clim Dyn*. doi:10.1007/s00382-011-1084-3
- Kleeman R, Moore AM (1997) A theory for the limitation of ENSO predictability due to stochastic atmospheric transients. *J Atmos Sci* 54:753–767
- Kleeman R, Tang Y, Moore AM (2003) The calculation of climatically relevant singular vectors in the presence of weather noise. *J Atmos Sci* 60:2856–2868
- Larson S, Kirtman B (2013) The Pacific Meridional Mode as a trigger for ENSO in a high-resolution coupled model. *Geophys Res Lett* 40:3189–3194. doi:10.1002/grl.50571
- Lopez H, Kirtman BP, Tziperman E, Gebbie G (2013) Impact of interactive westerly wind bursts on CCSM3. *Dyn Atmos Oceans*. doi:10.1016/j.dynatmoce.2012.11.001
- Love G (1985) Cross-equatorial influence of winter hemisphere subtropical cold surges. *Mon Wea Rev* 113:1487–1498
- Moore AM, Kleeman R (1996) The dynamics of error growth and predictability in a coupled model of ENSO. *Quart J Roy Meteor Soc* 122:1405–1446
- Moore AM, Kleeman R (1999a) The nonnormal nature of El Niño and intraseasonal variability. *J Clim* 12:2965–2982
- Moore AM, Kleeman R (1999b) Stochastic forcing of ENSO by the intraseasonal oscillation. *J Clim* 12:1199–1220
- Murakami T, Sumathipala WL (1989) Westerly bursts during the 1982/83 ENSO. *J Clim* 2:71–85
- Nitta T (1989) Development of a twin cyclone and westerly bursts during the initial phase of the 1986–87 El Niño. *J Meteor Soc Jpn* 67:677–681
- Nitta T, Motoki T (1987) Abrupt enhancement of convective activity and low-level westerly burst during the onset phase of the 1986–87 El Niño. *J Meteor Soc Jpn* 65:497–506
- Penland C, Matrosova L (1994) A balance condition for stochastic numerical models with application to the El Niño–Southern Oscillation. *J Clim* 7:1352–1372
- Penland C, Sardeshmukh PD (1995) The optimal growth of tropical sea surface temperature anomalies. *J Clim* 8:1999–2024
- Reynolds RW, Smith TM (1994) Improved global sea surface temperature analyses using optimum interpolation. *J Clim* 7:929–948
- Rogers JC (1981) The North Pacific Oscillator. *J Climatol* 1:39–57
- Schneider EK, Fan M (2007) Weather noise forcing of surface climate variability. *J Atmos Sci* 64:3265–3280
- Thompson CJ, Battisti DS (2001) A linear stochastic dynamical model of ENSO. Part II: analysis. *J Clim* 14:445–466
- Timmermann A, Jin F–F, Abshagen J (2003) A nonlinear theory for El Niño bursting. *J Atmos Sci* 60:152–165
- Vimont D, Wallace J, Battisti D (2003a) The seasonal foot-printing mechanism in the Pacific: implication for ENSO. *J Clim* 16:2668–2675
- Vimont D, Battisti D, Hirst AC (2003b) The seasonal footprint mechanism in the CSIRO general circulation model. *J Clim* 16:2653–2667
- Wu R, Kirtman BP (2003) On the impact of the Indian summer monsoon on ENSO in a coupled GCM. *Quart J Roy Meteor Soc* 129:3439–3468
- Wu R, Kirtman BP (2004a) Impact of the Indian Ocean on the Indian summer monsoon-ENSO relationship. *J Clim* 17:3037–3054
- Wu R, Kirtman BP (2004b) Understanding the impacts of the Indian Ocean on ENSO variability in a coupled GCM. *J Clim* 17:4019–4031
- Wu Z, Schneider EK, Kirtman BP (2004) Causes of low frequency North Atlantic SST variability in a coupled GCM. *Geophys Res Lett* 31:L09210. doi:10.1029/2004GL019548
- Xue Y, Cane MA, Zebiak SE (1997) Predictability of a coupled model of ENSO using singular vector analysis. Part I: optimal growth in seasonal background and ENSO cycles. *Mon Wea Rev* 125:2043–2056
- Yeh S-W, Kirtman BP (2004a) The impact of atmospheric internal variability on the North Pacific SST variability. *Clim Dyn* 22:721. doi:10.1007/s00382-004-0399-8
- Yeh S-W, Kirtman BP (2004b) Decadal North Pacific sea surface temperature variability and the associated global climate anomalies in a coupled general circulation model. *J Geophys Res* 109:D20113. doi:10.1029/2004JD004785
- Yu L, Rienecker MM (1998) Evidence of an extratropical atmospheric influence during the onset of the 1997–98 El Niño. *Geophys Res Lett* 25:3537–3540
- Yu L, Weller RA, Liu TW (2003) Case analysis of a role of ENSO in regulating the generation of westerly wind bursts in the western equatorial Pacific. *J Geophys Res* 108:3128. doi:10.1029/2002JC001498
- Zavala-Garay J, Moore AM, Perez CL, Kleeman R (2003a) The response of a coupled model of ENSO to observed estimates of stochastic forcing. *J Clim* 16:2827–2842
- Zavala-Garay J, Moore AM, Kleeman R (2003b) Influence of stochastic forcing on ENSO prediction. *J Geophys Res* 109:C11007. doi:10.1029/2004JC002406
- Zavala-Garay J, Zhang C, Moore AM, Kleeman R (2005) The linear response of ENSO to the Madden–Julian Oscillation. *J Clim* 18:2441–2459
- Zavala-Garay J, Zhang C, Moore AM, Wittenberg AT, Harrison MJ, Rosati A, Vialard J, Kleeman R (2008) Sensitivity of hybrid ENSO models to unresolved atmospheric variability. *J Clim* 21:3704–3721
- Zhang C, Gottschalck J (2002) SST anomalies of ENSO and the Madden–Julian oscillation in the equatorial Pacific. *J Clim* 15:2429–2445
- Zhang Li, Chang Ping, Tippet Michael K (2009a) Linking the Pacific meridional mode to ENSO: utilization of a noise filter. *J Clim* 22:905–922
- Zhang T, De-Zhen S, Neale R, Rasch P (2009b) An evaluation of ENSO asymmetry in the community climate system models: a view from the subsurface. *J Clim* 22:5933–5961